Monthly Notices
of the
ROYAL ASTRONOMICAL SOCIETY

Mon. Not. R. Astron. Soc. **399,** 2004–2020 (2009) doi:10.1111/j.1365-2966.2009.15406.x

Effects of ram pressure on the gas distribution and star formation in the Large Magellanic Cloud

Chiara Mastropietro,[1,2]★ Andreas Burkert[2] and Ben Moore[3]

[1]*LERMA, Observatoire de Paris, UPMC, CNRS, 61 Av. de l'Observatoire, 75014 Paris, France*
[2]*Universitäts Sternwarte München, Scheinerstr. 1, D-81679 München, Germany*
[3]*Institute for Theoretical Physics, University of Zürich, CH-8057 Zürich, Switzerland*

Accepted 2009 July 15. Received 2009 July 13; in original form 2009 May 6

ABSTRACT

We use high-resolution *N*-body/smoothed particle hydrodynamics (SPH) simulations to study the hydrodynamical interaction between the Large Magellanic Cloud (LMC) and the hot halo of the Milky Way. We investigate whether ram pressure acting on the satellite's interstellar medium can explain the peculiarities observed in the H I distribution and the location of the recent star formation activity.

Due to the present nearly edge-on orientation of the disc with respect to the orbital motion, compression at the leading edge can explain the high density region observed in H I at the south-east border. In the case of a face-on disc (according to Mastropietro the LMC was moving almost face-on before the last perigalactic passage), ram pressure directed perpendicular to the disc produces a clumpy structure characterized by voids and high density filaments that resemble those observed by the Parkes H I survey. As a consequence of the very recent edge-on motion, the Hα emission is mainly concentrated on the eastern side where 30 Doradus and most of the supergiant shells are located, although some Hα complexes form a patchy distribution on the entire disc. In this scenario, only the youngest stellar complexes show a progression in age along the leading border of the disc.

Key words: hydrodynamics – methods: *N*-body simulations – galaxies: individual: LMC – galaxies: interactions.

1 INTRODUCTION

The Large Magellanic Cloud (LMC) has revealed a very complex structure both in the stellar and in the gaseous components. The elongation of the stellar disc in the direction of the Galactic Centre, its substantial vertical thickness, the warp and the strong asymmetric bar are naturally predicted by numerical simulations as a result of the gravitational interaction between the LMC and the Galaxy (Bekki & Chiba 2005; Mastropietro et al. 2005, hereafter M05). The old stellar distribution appears to be quite smooth in the outer parts of the disc, with no signs of spiral structures out to a radius of 10 kpc (van der Marel 2001). Within the same radius, the H I large-scale structure reveals the presence of several asymmetric features that have no equivalent in the old stellar disc. The gaseous disc is characterized by the presence of an elongated region located at the south-east of the galaxy and aligned with the border of the optical disc, where the column density distribution shows a steep increase (Putman et al. 2003; Staveley-Smith et al. 2003). Since the LMC proper motion vector is directed to the east, it appears natural to associate this high density region with ram pressure acting on the leading edge of the disc due to the orbital motion of the LMC and its consequent interaction with the diffuse hot gas in the halo of the Milky Way (MW).

The presence of an extended hot halo surrounding galaxies and in hydrostatic equilibrium within the dark matter potential is expected by current models of hierarchical structure formation (Maller & Bullock 2004). In the MW, X-ray absorption lines produced by hot ($T \sim 10^6$ K) gas are detected in the spectra of several bright active galactic nuclei (AGN; Williams et al. 2005; Fang et al. 2006). Some ionization features discovered in the Magellanic Stream and high velocity Clouds indicate that this distribution of hot gas extends well beyond the Galactic disc (>70 kpc). Constraints from dynamical and thermal arguments fix its density in a range between 10^{-5} and 10^{-4} cm^{-3} at the LMC distance from the Galactic Centre (but Kaufmann et al. 2009 suggest a value 10 times higher).

Cioni et al. (2006) have performed a detailed analysis of the LMC global star formation rate (SFR) using asymptotic giant branch stars. They find an irregular and patchy distribution in age, with the youngest carbon-rich systems located at the south-east of the disc. The present SF activity is rather clumpy and concentrated in stellar complexes characterized by intense H II emission and

★E-mail: chiara.mastropietro@obspm.fr

associated with bright Hα filamentary bubbles. Most of these very young structures lie on the south-east of the disc, in the proximity of 30 Doradus, the largest star-forming region of the LMC, some are located in the bar and the remainder form an asymmetric pattern that covers the entire disc with no apparent relation to the global geometry of the satellite.

It is not clear which is the overall physical mechanism responsible for triggering SF with the observed asymmetric pattern, and different models have been proposed in the past. The stochastic self-propagating star formation (SSPSF) model (Gerola & Seiden 1978) predicts a clear age gradient in the LMC's stellar complexes, with the edges being younger with respect to the centre, in contradiction with observations (Braun et al. 1997). de Boer et al. (1998) proposed a scenario where the bow shock originated by the motion of the LMC through the hot galactic halo compresses the leading edge of the disc and induces SF. The pressure at the south-eastern edge of the LMC is indeed 10 times higher than the average in the rest of the LMC (Blondiau et al. 1997). This model, which assumes the orbital motion vector lying in the plane of the disc, predicts increasing ages of the stellar complexes in the direction of the rotation, due to the fact that the material compressed at the front side of the disc moves, in time, away to the side. The youngest systems would indeed lie at the south-east border of the disc, where the relative velocity between the corotating interstellar medium and the external diffuse gas is maximum. Several giant structures along the outer east and north edge of the LMC actually show a progression in age in a clockwise direction: moving from south-east to the north LMC 2, 30 Doradus and LMC 3, LMC 4, NGC 1818. In particular, the difference in age between 30 Doradus and LMC 4 is exactly their distance along the border of the disc divided by the satellite's rotational velocity (Harris, private communication). Grebel & Brandner (1998) studied the recent SF history of the LMC using Cepheids and other supergiant stars and found that although the majority of the SF events in the last 30 Myr are concentrated on the east border, others are distributed across the entire disc in partial contrast with the bow-shock-induced SF model, that cannot explain them.

In this work, we use high-resolution smoothed particle hydrodynamics (SPH) simulations to study the effects of the interaction between the LMC interstellar medium and the diffuse hot halo of the MW. We want to investigate whether the ram pressure acting on the leading edge of the LMC disc is responsible for the increase in density observed in the south-east and for triggering SF. The analytic model of de Boer et al. (1998) assumes a pure edge-on model, but according to van der Marel et al. (2002) the present angle between the LMC disc and the orbital motion is nearly 30°. Even in the absence of precession and nutation, this angle is subjected to large variations during the orbital period in such a way that compression produced by the external hot gas can affect in time both edge-on and face-on.

Moreover, the ram pressure felt by the LMC is not constant and has a maximum when the satellite approaches the perigalacticon. The motion of the LMC through the hot halo of the MW during the last 1 Gyr is modelled using 'test wind tunnel' simulations with increasing ram-pressure values.

The paper is structured as follows. Section 2 describes the models and the SF criteria adopted, Section 3 illustrates the results of simulations without SF, focused on the investigation of pure effects of compression on the LMC interstellar medium, while Section 4 describes the runs where SF is activated. Several simulations have been performed, assuming different SF models, disc inclinations and hot halo densities.

Table 1. Galaxy model: for each component mass (in units of $10^{10}\,M_\odot$) and scale radius (in kpc) are indicated. The gaseous disc has exponential and extended components. R_d is defined as in equation (1), while the scale radius of the NFW profile is $r_s = r_{vir}/c$, where r_{vir} and c are the virial radius and concentration, respectively. The last three columns report the number of particles, mass particle (in units of $10^5\,M_\odot$) and softening length (in kpc).

	Mass	Scale radius	N	m	ϵ
Gas exp. disc	0.055	1.66	5×10^4	0.11	0.1
Gas ext. disc	0.055		5×10^4	0.11	0.1
Stellar disc	0.11	1.66	5×10^4	0.22	0.1
DM halo	2.38	6.02	6×10^5	10.4	0.5

2 SIMULATIONS

2.1 Galaxy model

The initial conditions of the simulations are constructed using the technique described by Hernquist (1993). Our disc galaxy model (see Table 1) is a multicomponent system with a stellar and gaseous disc embedded in a spherical NFW (Navarro, Frenk & White 1997) dark matter halo. The density profile of the dark matter halo is adiabatically contracted in response to baryonic infall (Blumenthal et al. 1986). The stellar disc follows an exponential surface density profile of the form

$$\Sigma(R) = \frac{M_d}{2\pi {R_d}^2} \exp(-R/R_d), \quad (1)$$

where M_d and R_d are the disc mass and radial scalelength (in cylindrical coordinates), respectively, while the thin vertical structure has a scalelength $z_d \sim \frac{1}{5} R_d$:

$$\rho_d(R, z) = \frac{\Sigma(R)}{2 z_d} \operatorname{sech}^2(z/z_d). \quad (2)$$

The gaseous disc is characterized by an exponential profile with the same radial and vertical scalelength as the stellar component and by a constant density layer which extends up to $8R_d$. Half of the LMC's gaseous mass lies in this extended disc (Fig. 1). The vertical structure of the disc is in hydrostatic equilibrium with the global potential of the galaxy.

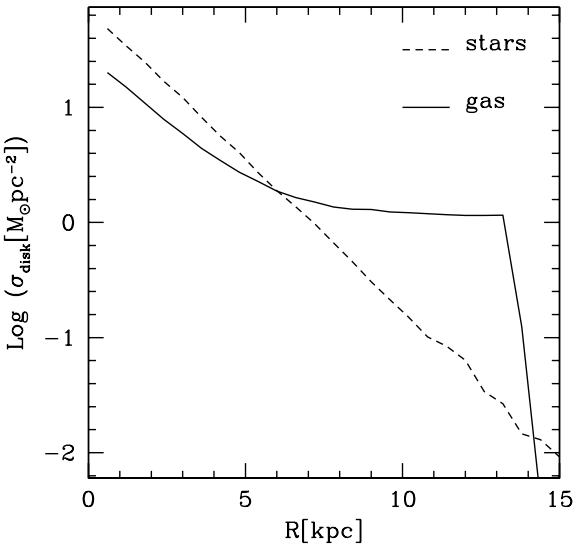

Figure 1. Gaseous and stellar disc surface density profiles (cylindrical coordinates).

The structural parameters of the disc and the halo are chosen so that the resulting rotation curve resembles that of a typical bulgeless late-type (Sc/Sd) disc galaxy (Courteau 1997; Persic & Salucci 1997). They are similar to those adopted in M05 for the initial LMC model and reproduce quite well the peak of the rotation curve inferred by van der Marel et al. (2002) (Fig. 1). As seen in M05, the interaction with the MW does not affect significantly the stellar and dark matter mass in the inner 8–9 kpc of the LMC and consequently the global rotation curve within this radial range. The choice of an extended gaseous component for the initial LMC model is motivated by the fact that spiral galaxies in the local Universe are commonly observed to be embedded in extended discs of neutral hydrogen significantly larger than their stellar component (Hunter & Gallagher 1985; Broeils & van Woerden 1994). As seen in M05, the combined effect of tidal interactions and ram-pressure stripping can remove a significant fraction of gas from an LMC disc orbiting within the hot halo of the MW, with a ram-pressure stripping radius which is a factor of 3 smaller than the initial radius of the gaseous disc. Also in the case of an LMC with orbital velocities significantly higher (Mastropietro 2008), hydrodynamic and gravitational forces together are effective in resizing and reshaping the extended gaseous disc of the satellite beyond 8 kpc. In the present work, we neglect the presence of gravitational forces focusing on the effects of pure ram pressure. Therefore, we do not expect to see a significant decrease in the radius of the gas distribution. However, in order to take into account the loss of cold gas from the disc of the satellite and the SF events, we assumed an initial amount of gas in the disc which is about three times larger than the H I mass in the LMC ($2.9 \times 10^8\,\mathrm{M}_\odot$ according to Putman et al. 2003).

The mass within the virial radius is set equal to $2.18 \times 10^{10}\,\mathrm{M}_\odot$ and the fraction of mass in the disc is $\sim$10 per cent, equally distributed between the gaseous and stellar components. The contribution of the different components to the global rotation curve, assuming a disc scalelength $R_\mathrm{d} = 1.7$ kpc and a dark halo concentration $c = 9.5$ (where c is defined as $c = r_\mathrm{vir}/r_\mathrm{s}$, with r_vir and r_s being the virial and scale radii of the NFW halo, respectively), is plotted in Fig. 2. The halo spin parameter, which sets the disc scalelength in our modelling, is $\lambda = 0.074$, where λ relates the angular momentum J to the total energy E of a system with virial mass M_vir through the relation $\lambda = J|E|^{1/2}G^{-1}M_\mathrm{vir}^{-5/2}$.

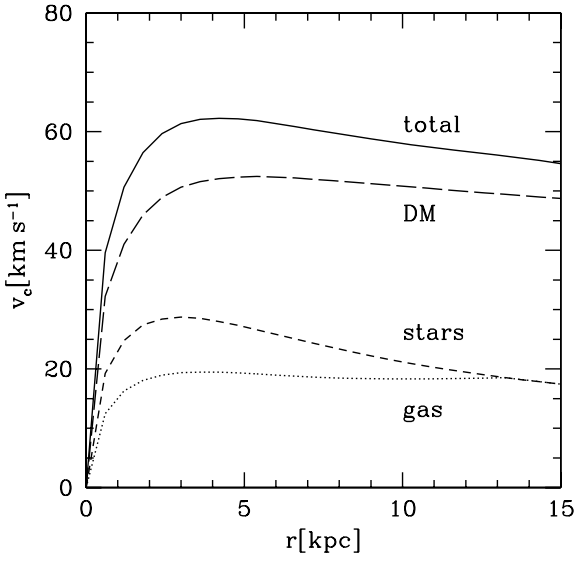

Figure 2. Galaxy model rotation curves.

The initial stellar disc of the satellite galaxy has, within its scale radius R_d, a central mass surface density of $\sim 35\,\mathrm{M}_\odot\,\mathrm{pc}^{-2}$ (Fig. 1), that corresponds to a B-band surface brightness of $\sim$24 mag arcsec^{-2}, assuming a mass-to-light ratio of $\simeq 2$. The central gas surface density is only $\sim 16\,\mathrm{M}_\odot\,\mathrm{pc}^{-2}$ since a significant fraction of gas is distributed in the external disc. Assuming 72 per cent H I abundance, this value corresponds to a hydrogen column density of $\sim 1.5 \times 10^{21}$ within R_d, comparable with the values observed by Staveley-Smith et al. (2003) with the LMC Parkes multibeam H I survey.

2.2 Stability criterion

In order to obtain a strongly stable disc against bar formation even in the presence of significant gas stripping and consequent perturbation of the satellite potential, the thickness of the stellar component is set such that Toomre's (Toomre 1964) stability criterion is largely satisfied. In particular, Toomre's parameter for the stellar disc,

$$Q_s(R) = \frac{\sigma_\mathrm{r}(R)\kappa(R)}{3.36 G \Sigma_s(R)}, \tag{3}$$

where $\sigma_\mathrm{r}(R)$ is the radial velocity dispersion, $\kappa(R)$ is the local epicyclic frequency and $\Sigma_s(R)$ is the unperturbed stellar surface density, has a minimum at the disc scalelength with $Q_s(R_\mathrm{d}) \sim 4$. For a gaseous disc, the stability of the disc is expressed in terms of the gas sound speed v_s and surface density $\Sigma_g(r)$ through the relation

$$Q_g(R) = \frac{v_s \kappa(R)}{\pi G \Sigma_g(R)}. \tag{4}$$

The gaseous disc has initially a constant temperature of 10 000 K, which implies $Q_g(R) > 3$ and $Q(R_\mathrm{d}) = 3.2$.

According to Jog & Solomon (1984) and Rafikov (2001), the stability of a multicomponent disc is not guaranteed by the individual stability of its single constituents, due to the mutual gravitational interaction between the gas and stars. Stars are characterized by velocity dispersions three to four times larger than the typical sound velocities in the cold gaseous disc and even relatively small variations of the gaseous component parameters can significantly affect the stability of the whole disc (Jog & Solomon 1984). Therefore, we choose a large value of Q to contrast the effects of ram pressure. In the case of a two-component – gaseous and stellar – disc, the stability condition is expressed by (Jog & Solomon 1984)

$$Q_\mathrm{tot} = \left[\frac{2}{Q_s}\frac{\pi}{3.36}\frac{q}{1+q^2} + \frac{2}{Q_g}x\frac{q}{1+q^2x^2} \right]^{-1} > 1, \tag{5}$$

where $q = k\sigma_s/\kappa$ and $x = c_g/\sigma_s$. Fig. 3 illustrates the dependence of Q_tot on the dimensionless wavenumber of the perturbation q within three different regions of the disc: at the disc scalelength R_d, at $R =$ 5 kpc and in the external region ($R = 8$ kpc), where the gas component predominates. The Jog & Solomon (1984) criterion is always satisfied and the disc is stable against axisymmetric perturbations, independently of their wavelength. In order to check stability, the disc was initially evolved in isolation for 1 Gyr.

2.3 Star formation recipes

All the simulations we now discuss were carried out using GASOLINE, a parallel tree-code with multistepping (Wadsley, Stadel & Quinn 2004) which is an extension of the pure N-body gravity code PKDGRAV developed by Stadel (2001). The code uses a spline kernel with compact support (Monaghan & Lattanzio 1985) where the interaction distance for a particle i is set equal to two times the

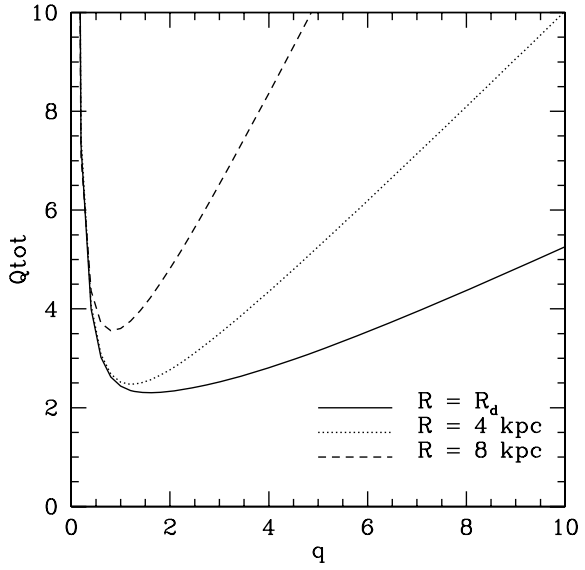

Figure 3. Total stability parameter $Q_{\rm tot}$ of the disc (see equation 5) versus the dimensionless wavenumber $q = k\sigma_s/\kappa$ of the perturbation. $Q_{\rm tot}$ is calculated for three different radii of the disc.

smoothing length h_i, defined as the kth neighbour distance from the particle. In this paper, $k = 32$. The internal energy of the gas is integrated using the antisymmetric formulation of Evrard (1988) that conserves entropy closely. Dissipation in shocks is modelled using the quadratic term of the standard Monaghan (1992) artificial viscosity. The Balsara (Balsara 1995) correction term is used to suppress the viscosity in non-shocking, shearing environments. The code includes radiative cooling for a primordial mixture of hydrogen and helium in collisional equilibrium. At temperatures below 10^4 K, the gas is entirely neutral and due to the lack of molecular cooling and metals, the efficiency of the cooling function drops rapidly to zero. We used an SF recipe that includes density and temperature criteria, while the converging flow criterion is not required in most of the simulations. Gas particles are eligible to form stars only if the density of the SF region has a minimum physical density corresponding to 0.1 hydrogen atoms per cm^3 (Summers 1993; Katz, Weinberg & Hernquist 1996) and an overdensity $\rho_{\rm gas}/\bar{\rho}_{\rm gas} > 55.7$ (Katz et al. 1996), which basically restricts SF to collapsed, virialized regions. The physical density threshold describes the steep drop in the SFR observed in disc galaxies when the gas surface density is much lower than a critical value $\Sigma_{\rm c}$ (Kennicutt 1989). The density threshold $\rho_c = 0.1\,{\rm cm}^{-3}$ is compatible with observational results. According to Katz (1992), the star-forming region has to be part of a converging flow that implies a local negative divergence of the SPH velocity field. However, the converging flow criterion was introduced to describe SF in cosmological simulations, where the geometry of the collapsing regions is approximatively spherical. In the case of SF regions such as 30 Doradus, localized at the periphery of the LMC disc where gas particles relatively close in distance can have significantly different kinematics, this criterion leads to underestimate of the SFR. Therefore, the converging flow is not required in most of the simulations. A single run including the converging flow requirement has been performed for comparison.

The SFR is assumed to be proportional to $\rho_{\rm gas}^{3/2}$ (Silk 1987), where $\rho_{\rm gas}$ represents the volume density of the cold gas, and is given by the expression (Katz et al. 1996)

$$\frac{{\rm d}\rho_\star}{{\rm d}t} = \frac{c_\star \rho_{\rm gas}}{t_{\rm form}}, \tag{6}$$

where the SF time-scale $t_{\rm form}$ is the maximum between the local gas dynamical collapse time $t_{\rm dyn} = (4\pi G\rho_{\rm gas})^{-1/2}$ and the local cooling time. If the gas is already cool enough to form stars, that is $T < T_{\rm max}$, then $t_{\rm dyn}$ is used. We assumed $T_{\rm max} = 30\,000$ K. The constant SFR parameter $c_\star$ is chosen such that we reproduce the global LMC SFR (Sandage 1986). Once a gas particle satisfies the above criteria, it spawns stars according to a probability distribution function. In particular, the probability p that a gas particle forms stars in a time Δt is modelled as

$$p = (1 - {\rm e}^{-c_\star \Delta t/t_{\rm form}}). \tag{7}$$

A random number is then drawn to determine whether the gas particle forms stars during Δt. For all the simulations in this paper, $\Delta t = 4$ Myr. The newly created collisionless particle has the same position, velocity and softening length as the original gas particle while its mass is a fixed fraction ϵ of the parent gas particle, whose mass is reduced accordingly. Following Katz (1992), we assumed for our favourite models an SF efficiency $\epsilon = 1/3$. Up to six particles are then created for each gas particle in the disc. After its mass has decreased below 10 per cent of its initial value, the gas particle is removed and its mass is re-allocated among the neighbouring particles.

2.4 Test wind tunnels

In order to study the influence of pure ram pressure on a galaxy model orbiting in an MW halo, we performed 'wind tunnel' simulations where the ram-pressure value varies with time (for a similar study, see also Roediger & Brüggen 2007).

We represent the hot gas as a flux of particles moving along the major axis of an oblong of base equal to the diameter of the dark matter halo of the satellite and height $h = vt$, where v is the velocity of the LMC at the perigalacticon and t is the time-scale of the simulation. The hot particles have an initial random distribution and a temperature $T = 10^6$ K. The box has periodic boundary conditions in order to restore the flow of hot gas that leaves the oblong. The galaxy model is at rest at the centre of the oblong.

Kinematical data (van der Marel et al. 2002) indicate that the LMC, presently located at ∼50 kpc from the Galactic Centre, is just past a perigalactic passage and has an orbital velocity of about 300 km s^{-1}. Recent proper motion measurements by Kallivayalil et al. (2006) and Piatek, Pryor & Olszewski (2008) suggest that the velocity of the satellite is substantially higher (almost 100 km s^{-1}) than previously estimated and consistent with the hypothesis of a first passage about the MW (Besla et al. 2007). In both scenarios, the Cloud is affected by the largest ram-pressure values during the last million years of its orbital evolution. Indeed, while in the models proposed by Besla et al. (2007) the LMC does not enter the halo of the MW earlier than 1 Gyr (slightly different orbits are found in Mastropietro 2009), in M05 we have shown that the change in the orbital parameters due to dynamical friction strongly affects the ram-pressure stripping rate. Even in the case of a 'low velocity' model, the largest ram pressure on the satellite is expected during the last orbital semiperiod (about 1 Gyr) due to the increasing velocity and external gas density.

We followed ram pressure acting on the LMC's intergalactic medium (IGM) during the past 1 Gyr. The density of the hot external gas increases with time (the mass of hot particles in the tube grows at each time-step), in such a way that in our low velocity model the external pressure experienced by the cold disc varies from $P_{\rm min} = \rho_{\rm min} v_{\rm min}^2 = 5 \times 10^{-15}$ dyn cm^{-2} to $P_{\rm max} = 1.52 \times 10^{-13}$ dyn cm^{-2} at

the time corresponding to the pericentric passage. This is equivalent to assuming $v_{\rm min} = 170\,{\rm km\,s^{-1}}$ and $v_{\rm max} \sim 300\,{\rm km\,s^{-1}}$, and a number density of the external gas that increases from $\sim 10^{-5}\,{\rm cm^{-3}}$ to $10^{-4}\,{\rm cm^{-3}}$ at $\sim$50 kpc from the Galactic Centre. These density values are comparable with those provided by M05, who modelled the MW hot halo assuming a spherical distribution of gas that traces the dark matter profile, with a mean number density of 2×10^{-5} within 150 kpc. We also consider the eventuality of a less dense Galactic halo and performed runs where the gas density is a factor of 10 lower. Models with higher velocities (Kallivayalil et al. 2006) and orbital parameters similar to those suggested by Besla et al. (2007) are also explored. In detail, $P_{\rm min}$ is the same as in the low velocity models since the higher orbital velocity at the beginning of the simulation (about $250\,{\rm km\,s^{-1}}$) is compensated by a lower external density ($\sim 5 \times 10^{-6}\,{\rm cm^{-3}}$, according to Mastropietro 2009; indeed, 1 Gyr ago the satellite has just passed through the virial radius of the MW). The maximum pressure felt by the disc is $P_{\rm max} = 2.67 \times 10^{-13}\,{\rm dyn\,cm^{-2}}$, which corresponds to a Cloud moving with $v_{\rm max} \sim 400\,{\rm km\,s^{-1}}$ through an external hot medium of density $10^{-4}\,{\rm cm^{-3}}$.

Each galaxy model is simulated using 750 000 particles, of which 6×10^5 are in the dark halo and 1.5×10^5 in the disc (10^5 collisional and 5×10^4 collisionless). The hot gas in the 'wind tunnel' has 2×10^6 particles, in such a way that the mass ratio $m_h/m_{\rm disc}$ between hot particles and particles in the disc is close to unity even when the halo density is the largest. This choice permits us to avoid the presence of scattering and numerical holes which artificially change the shape of the front edge and influence the morphology of the disc (M05). The gravitational spline softening is set equal to 0.5 kpc for the dark halo and the hot gas in the oblong, while it is 0.2 kpc for stars and gas in the disc.

3 COOLING SIMULATIONS

In order to study the effect of pure compression on the density distribution of cold gas in the LMC disc, we have run a first set of simulations where the gas cools radiatively but SF was not activated.

According to van der Marel et al. (2002) and Kallivayalil et al. (2006), the present angle between the LMC's disc and its proper motion vector is roughly 30°. Even neglecting the effects of precession and nutation on the disc plane of the satellite (van der Marel et al. 2002) this angle is expected to vary significantly during an orbital period, especially in the proximity of a pericentric passage due to rapid changes in the velocity vector. Different relative orientations of the disc with respect to the orbital motion are therefore investigated. The inclination angle i is defined as the angle between the angular momentum vector of the disc and the flux of hot particles in the wind tube, so that a galaxy moving edge-on through the external medium is characterized by $i = 90°$, while the observed LMC disc would have $i \sim 60°$. We explored cases with an inclination angle i of 90, 45 and 10° (runs cool90, cool45 and cool10, respectively).

With a hot halo temperature of 10^6 K, the relative velocity between the satellite and the external medium is supersonic (sound speed $\sim 135\,{\rm km\,s^{-1}}$ and Mach number $\mathcal{M} = 2.2$ and 3 at the pericentre of the low and high velocity orbits, respectively) and a bow shock forms in front of the disc (Fig. 4). Since the cooling time of the post-shock gas is $\sim$16 Gyr, the shock can be considered non-radiative and hydrodynamical quantities at the two sides of the shock front are in first approximation related by the Rankine–Hugoniot equations for a stationary normal shock.

For $\mathcal{M} > 1$ the jump conditions give $\rho_1/\rho_2 = v_2/v_1 < 1$ and $T_1 < T_2$, where subscripts 1 and 2 denote upstream and downstream

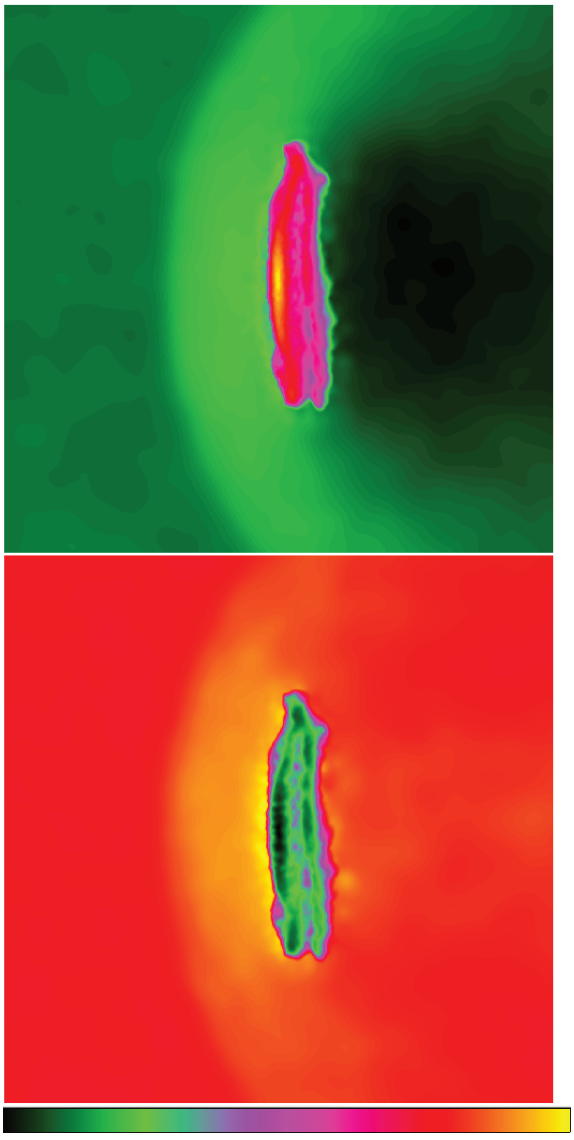

Figure 4. Density (upper panel) and temperature (bottom) map of a $50 \times 50\,{\rm kpc^2}$ region around the satellite, which is moving towards the left of the page nearly face-on (inclination angle $i = 10°$, cool10). Logarithmic colour scaling is indicated by the key at the bottom of the figure. The surface density map ranges between $\sim 2 \times 10^3$ (black) and $\sim 2 \times 10^9\,{\rm M_\odot\,kpc^{-2}}$ (yellow), while temperatures vary from 10^4 (black) to 10^7 K (yellow).

quantities, respectively. The ram pressure $P_2 = \rho_2 v_2^2$ actually felt by the galaxy behind the shock front is therefore smaller than that which it would suffer due to the upstream flux of hot particles, but conservation of the momentum flux across the shock discontinuity implies that the reduction in dynamical pressure has to be balanced by an increase in thermal pressure (see also Rasmussen, Ponman & Mulchaey 2006).

Fig. 5 illustrates the behaviour of hydrodynamical quantities across the shock discontinuity for a snapshot corresponding to the perigalacticon of a low velocity orbit. The disc inclination is $i = 10°$. The horizontal axis is centred on the LMC stellar disc and oriented perpendicular to the bow-shock nose, with the shock located at $x \sim 10$ kpc and the satellite moving towards increasing values of x. The Mach number derived by the temperature jump (between $x = 9.5$ and 12.5 kpc) is $\mathcal{M} = 2.1$, in good agreement with the theoretical value for a normal shock. Only hot halo particles are considered in

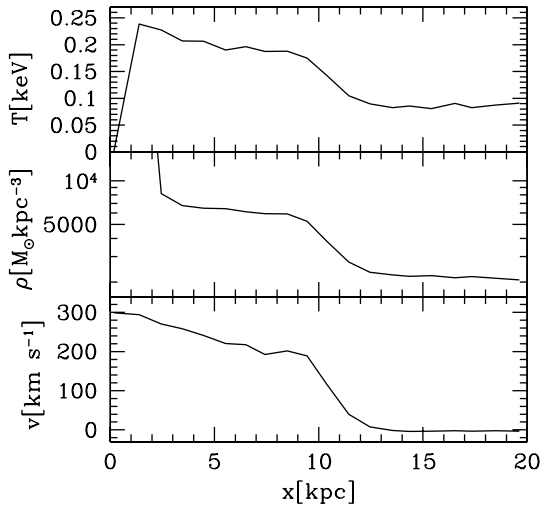

Figure 5. Gas temperature (top panel), density (middle) and one-dimensional velocity (bottom) profiles across the shock discontinuity.

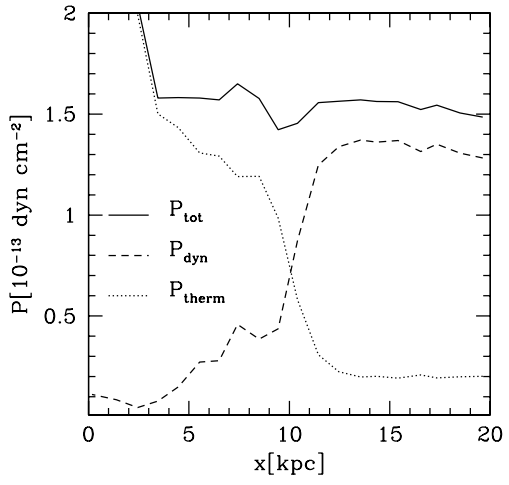

Figure 6. Dynamical ($P_{\rm dyn}$), thermal ($P_{\rm therm}$) and total ($P_{\rm tot}$) pressure across the shock.

computations but, due to the SPH nature of the simulations, close to the border of the disc we observe a further density increase and a sharp drop in temperature. The x-velocity profile is plotted in the system of reference where the pre-shock gas is at rest.

Pressure profiles across the shock are plotted in Fig. 6, where $P_{\rm dyn}$ is defined as ρv^2. The total pressure remains roughly constant until the edge of the disc. The steep increase at $x = 2.5$ kpc is due to the rapid growth in density at the border of the disc, which is not immediately followed by a decrease in temperature.

For $i > 0^\circ$, the shock wave is inclined with respect to the initial flow velocity and the Rankine–Hugoniot conditions apply to the normal components of the velocity across the shock discontinuity, while the component parallel to the shock front remains unchanged. The flow is therefore deflected towards an oblique shock wave and the jump at the shock discontinuity is smaller.

An edge-on ($i = 90^\circ$) disc behaves like a wedge moving supersonically with the vertex facing upstream. If the wedge angle is smaller than or equal to the maximum flow deflection angle, the oblique shock becomes attached to the vertex of the wedge and the flow is deflected so that the streamlines are parallel to the surfaces of the wedge. The shock standoff distance thus depends on the external density profile of the collisional edge-on disc and on the Mach number of the incident flow. In both low and high velocity edge-on models, the shock results almost attached to the disc.

Figs 7–9 illustrate – for different values of the inclination angle i – changes in the disc gas density distribution as the satellite passes through increasing values of the external pressure, moving towards the perigalacticon. Each couple of panels illustrates the state of the disc at increasing (from the top to the bottom) times along the orbit. Panels on the left represent H I column density maps. The density contrast is chosen in order to highlight the density gradient in the external disc, since the gas distribution in the central regions of the LMC is dominated by the presence of the bar and a direct comparison with pure ram-pressure simulations is not possible. The colour scale is logarithmic, with white corresponding to a density larger than 1.2×10^{21} cm^{-2} and blue to values lower than 5×10^{19} cm^{-2}. Hot gas particles flow on to the disc from the left to the right of each plot, with increasing ram-pressure values from the first to the fourth image. The disc is seen face-on and rotating clockwise. In the case of the edge-on run (Fig. 7) cold gas particles lying in the left-bottom quadrant of the disc feel the largest ram pressure, due to the fact that their relative velocity with respect to the external medium is maximum. The rotational velocity of the external disc is $\sim$55 km s^{-1}, which implies a relative velocity at the pericentre of $\sim$350 km s^{-1} (450 km s^{-1} in the case of a high velocity orbit). Panels on the right represent the change in mean density and radius of the gaseous external disc as a function of the azimuthal angle ϕ. Referring to the geometry of the H I density images on the left, $\phi = 0^\circ$ corresponds to the bottom of the disc and increases clockwise in such a way that the disc moves in the direction of $\phi = 90^\circ$. The gas density and the mean radius are both calculated within sections of a three-dimensional annulus with internal and external radii equal to 7 and 15 kpc, respectively. The initial azimuthal profiles (not represented in the plots) are flat since both these quantities have only radial dependence. As soon as the satellite starts moving through the surrounding medium, the external gas density develops a peak centred on $\sim\phi = 90^\circ$; disc particles localized in regions of maximum ram pressure get compressed and move on inner orbits, while their circular velocity increases consequently. After about a quarter of the orbital period, the gas has reached its minimum radius and maximum local density. The gaseous disc becomes strongly asymmetric: compression at the front edge produces a density increase along the left border of the disc, evident in the H I maps even at early times. The high density region forms a thin ($\sim$1.5 kpc) but continuous and well-defined arc which has not an equivalent in the stellar distribution. At the perigalacticon, this feature extends for almost 160° with a density more than one order of magnitude higher than gas located at smaller radii. Its average thickness ($\sim$1.5 kpc) and velocity dispersion along the line of sight are larger than the average values in the rest of the disc.

In the case of a satellite moving through the hot medium with an inclination angle different from 90°, the external pressure directed perpendicular to the plane of the disc increases as cos i (Roediger & Brüggen 2006) while compression at the leading edge is much less pronounced. Figs 8 and 9 refer to runs with inclination angles $i = 45^\circ$ and $i = 10^\circ$, respectively. Discs are shown face-on. The increment in density along the leading edge is smaller (cool45) than in the edge-on model and almost absent for $i = 10^\circ$ (cool10), while compression perpendicular to the plane of the disc produces local gravitational instabilities in the external gaseous disc (also Mayer, Mastropietro & Tran, in preparation). This effect is more evident in the nearly face-on run cool10 where high density filaments delimitate regions where the local density is almost one order of magnitude lower.

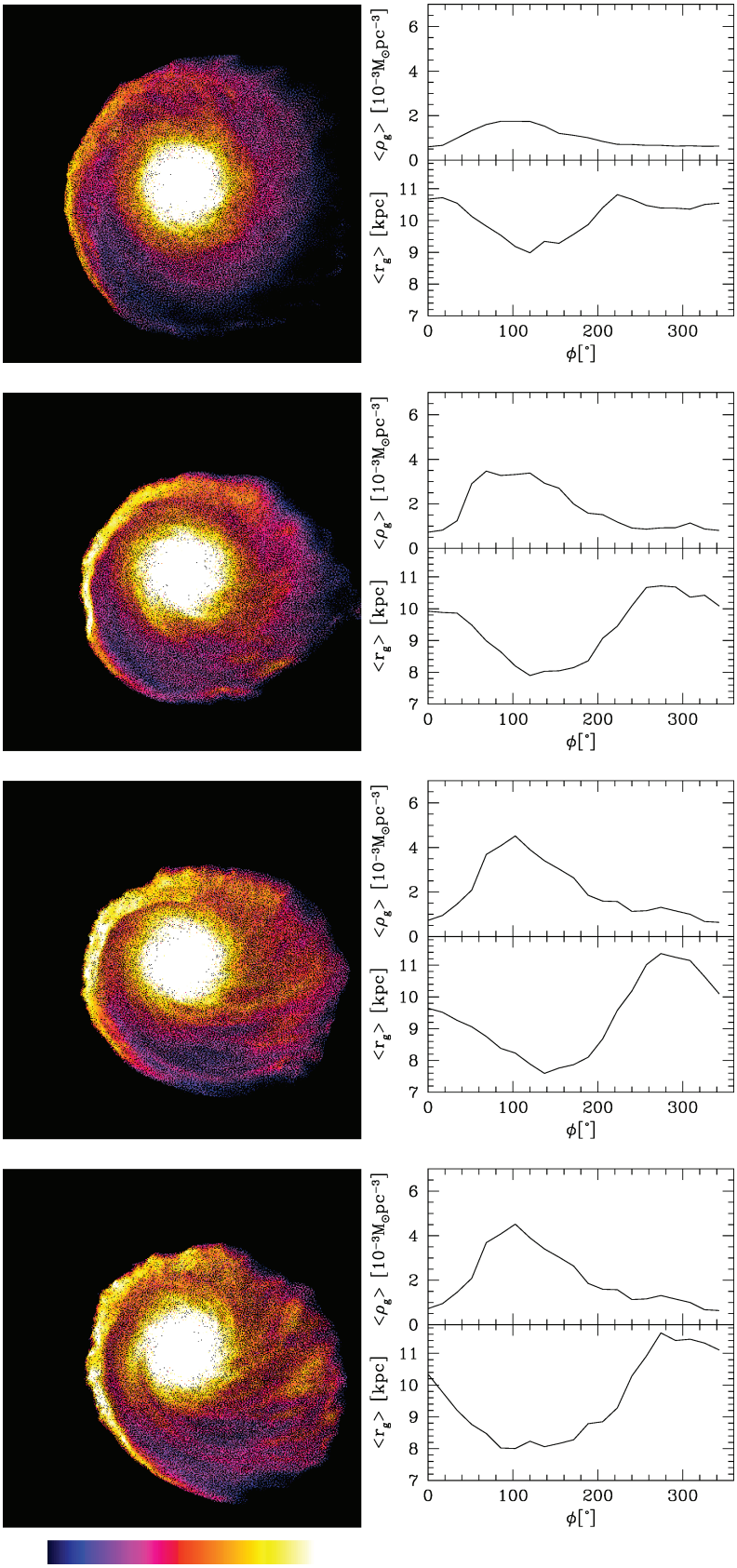

Figure 7. Edge-on model (run cool90). Evolution of the disc gas density distribution. Left-hand panels: H I column density maps (the galaxy is moving towards the left of the page). The colour scale is logarithmic with limits 5×10^{19} and 1.2×10^{21} cm^{-2}. Right-hand panels: mean gas density and radius of the external disc as a function of the azimuthal angle ϕ. Each pair of plots (from the top to the bottom) represents the state of the disc at increasing times along the orbit: Time = 0.4, 0.6, 0.8, 1 Gyr.

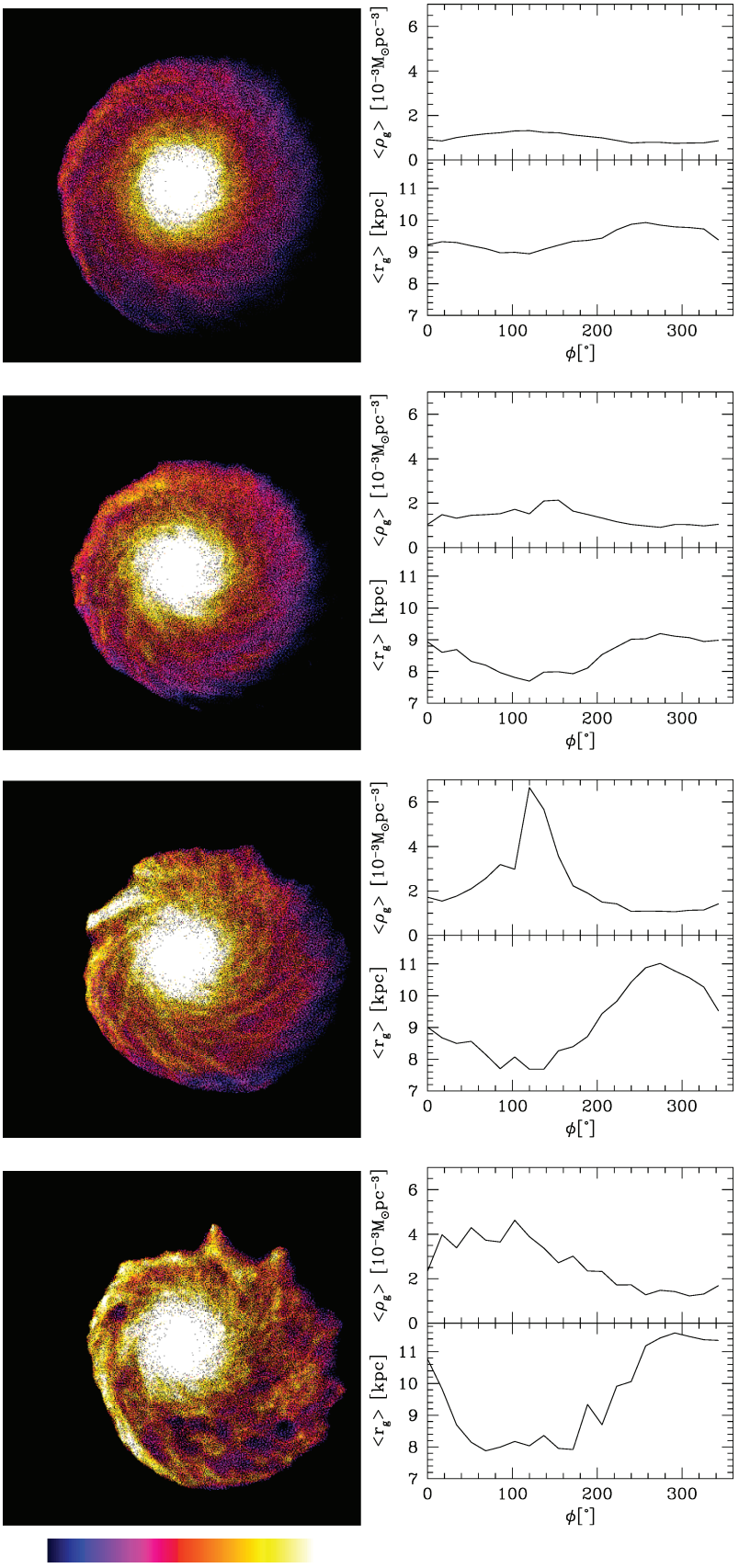

Figure 8. The same as in Fig. 7 for the model with inclination angle $i = 45^\circ$ (run cool45).

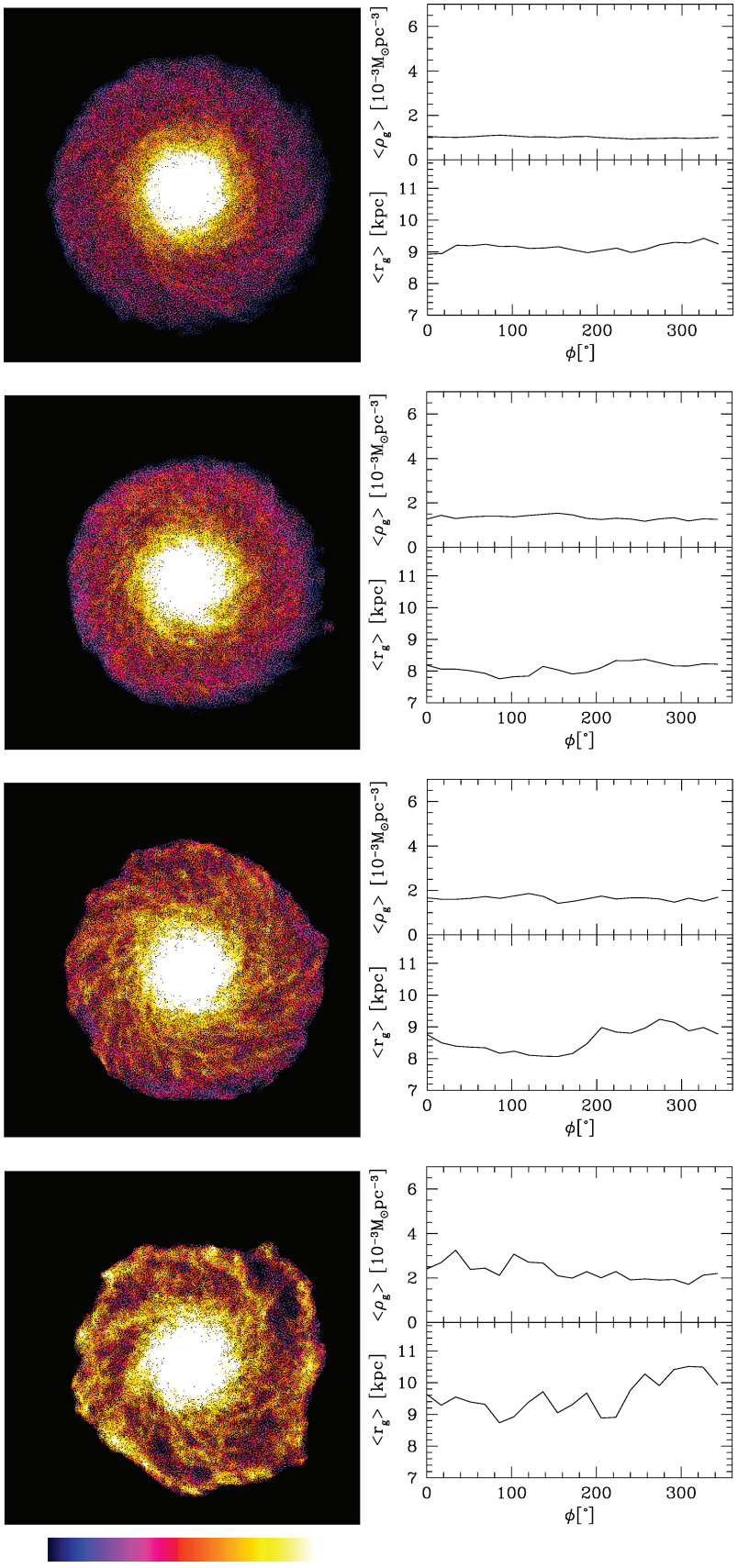

Figure 9. The same as in Fig. 7 for the model with inclination angle $i = 10^{\circ}$ (run cool10).

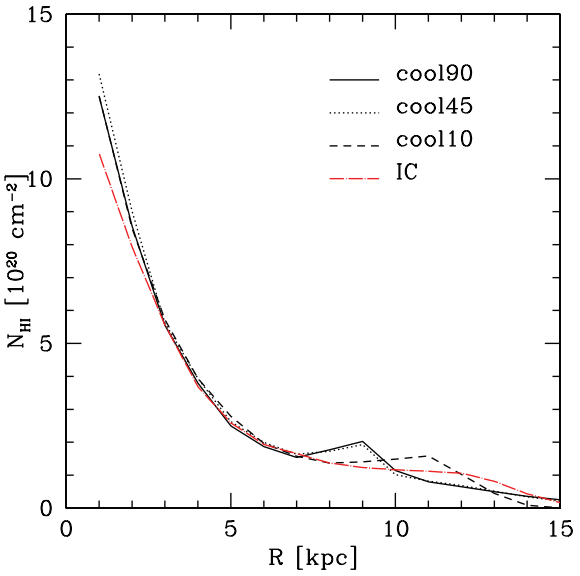

Figure 10. H I column density profile of the final LMC disc in units of 10^{20} cm^{-2}. The curves refer to different values of the inclination angle i. The red long-dashed line represents the column density profile of the initial disc.

Despite the absence of a peak in the azimuthal mean density profile, the integrated final density of cool10 is comparable to the other runs.

Fig. 10 represents the azimuthally averaged H I column density profile of the final disc configuration for the three simulations. As a result of the increase in density along the edge of the disc, the mean column density shows a secondary peak at large radius. A limb-brightened density profile has actually been observed by Staveley-Smith et al. (2003) using the Parkes multibeam H I survey of the LMC. The outer profiles of cool90 and cool45 are very similar, while in run cool10 the increment in density with respect to the original profile of the disc (long-dashed red curve in the plot) is located at larger radii (∼8.5 kpc). Indeed, due to compression of the leading edge the final gas distribution of cool90 and cool45 is asymmetric, the dense front edge being much closer to the centre than the opposite border of the disc. Therefore, the H I peak in the external disc is located at relatively small radii, while the azimuthally averaged gas distribution is more extended than in the case of the run cool10 since ram pressure elongates the back side of the disc. Again, we stress the fact that our gaseous disc is more extended than it would be in a fully self-consistent simulation including both gravitational and hydrodynamical forces. As seen in M05 and Mastropietro (2008) the combined effect of ram-pressure and tidal stripping is quite efficient in stripping gas from the outer satellite's disc, creating the tip of the Magellanic Stream already at large distances from the MW. The high density feature in cool90 would then form along the border of the disc at smaller radii and would not be easily subjected to further stripping due to the relatively ram-pressure values.

4 SIMULATIONS WITH STAR FORMATION

The compressive increase in H I density is naturally associated with excess SF. SPH simulations cannot follow the formation of molecular clouds but in first approximation, the molecular gas fraction can be related to the density of atomic gas (Vollmer et al. 2008).

The main parameters of SF simulations are summarized in Table 2.

As we already mentioned in Section 3, our standard SF model does not include the converging flow criterion and is characterized by an efficiency $\epsilon = 0.33$ (Katz 1992). The SFR parameter $c_\star$ is initially set equal to 0.02. This model was adopted to run wind tube simulations with inclination angles $i = 90^\circ, 45^\circ, 10^\circ$ (SF90, SF45, SF10) (Table 2). We also investigated different SF recipes requiring converging flows and assuming different values of $c_\star$ and ϵ. We explored SFR parameter values in the range from 0.01 to 0.05, that produce a SFR integrated over the entire disc comparable with 0.1 $M_\odot$ yr^{-1} provided by Sandage (1986). An efficiency $\epsilon = 1$ implies that whenever a gas particle satisfies the SF requirements, it is immediately turned into a single star particle of the same mass (Kaufmann et al. 2007).

Table 2. SF simulations. The second column indicates the use of the converging flow criterion in the SF recipe, the third and the fourth columns represent the SF efficiency ϵ and the SFR parameter $c_\star$ (equation 6), respectively, while i is the inclination angle of the disc, that is the angle between the angular momentum of the disc and the flux of hot particles. A model with $i = 90$ is indeed a disc moving edge-on in the external medium. The sixth and seventh columns represent the minimum and maximum ram pressure suffered by the satellite during its approach to the perigalacticon, respectively. The last column indicates the presence of a temperature floor for the disc gas.

Run	Conv	ϵ	$c_\star$	i (°)	$P_{\rm min}$ (10^{-13} dyn cm^{-2})	$P_{\rm max}$ (10^{-13} dyn cm^{-2})	$T_{\rm min}$ (K)
SF90	No	0.33	0.02	90	4.83×10^{-2}	1.50	0
SF45	No	0.33	0.02	45	4.83×10^{-2}	1.50	0
SF10	No	0.33	0.02	10	4.83×10^{-2}	1.50	0
SFconv	Yes	0.33	0.02	90	4.83×10^{-2}	1.50	0
SFϵ1	No	1	0.02	90	4.83×10^{-2}	1.50	0
SFconvϵ1	Yes	1	0.02	90	4.83×10^{-2}	1.50	0
SF90c0.01	No	0.33	0.01	90	4.83×10^{-2}	1.50	0
SF10c0.01	No	0.33	0.01	90	4.83×10^{-2}	1.50	0
SF90c0.05	No	0.33	0.05	90	4.83×10^{-2}	1.50	0
SF10c0.05	No	0.33	0.05	90	4.83×10^{-2}	1.50	0
SF90v400	No	0.33	0.02	90	4.83×10^{-2}	2.67	0
SF10v400	No	0.33	0.02	10	4.83×10^{-2}	2.67	0
SF10v400t12000	No	0.33	0.02	10	4.83×10^{-2}	2.67	1.2×10^4
SF10v400t15000	No	0.33	0.02	10	4.83×10^{-2}	2.67	1.5×10^4
SFld90	No	0.33	0.02	90	4.83×10^{-3}	1.5×10^{-1}	0
SFld10	No	0.33	0.02	10	4.83×10^{-3}	1.5×10^{-1}	0

In the last six simulations listed in Table 2, we used our standard SF model to investigate the effects of different orbital parameters and gas halo densities.

Runs SFv400 are characterized by a maximum ram-pressure value corresponding to a perigalactic velocity of $400\,\mathrm{km\,s^{-1}}$ (Kallivayalil et al. 2006). Such high velocity discs – when moving face-on through the external hot medium – are strongly affected by local instabilities and SF is consequently enhanced. The introduction of an artificial lower limit for the satellite gas temperature (in runs SF10v400t12000 and SF10v400t15000), higher than the cut-off in the cooling function, has the effect of reducing gravitational instabilities and fragmentation in the disc. This temperature threshold can be justified in order to crudely model the effect of the UV background and stellar feedback (Barnes 2002).

Finally, with simulations SF90ld and SF10ld in Table 2 we also consider the possibility of a Galactic hot halo 10 times less dense than our standard model.

Fig. 11 illustrates the state of the newly formed stellar disc at increasing times along the satellite orbit. Each couple of rows corresponds to one of the first three runs of Table 2 and is associated with a different inclination angle i. The first row of the pair represents the face-on projection of the disc with the galaxy moving towards the left of the page and the same geometry as in Fig. 7. Time increases from the left to the right. Each small cross indicates a new SF event at the time of the snapshot (within a time interval of 40 Myr) while the circle delimitates the external disc ($r > 7\,\mathrm{kpc}$). Stars form in the central regions as soon as the SF algorithm is activated, but here the SF activity of the inner disc is not represented. The second row represents the total mass $M_\star$ of the newly formed stars in the external disc as a function of the disc azimuthal angle ϕ.

In the case of a galaxy moving edge-on through the external medium (SF90), stars form at the leading edge of the disc when the ram pressure becomes larger than $\sim 5 \times 10^{-14}\,\mathrm{dyn\,cm^{-2}}$, at Time $\sim$0.3 Gyr. The location of the SF events initially corresponds to the H I column density peak observed in cool90 around 100° (Fig. 7). Later on it expands along the entire front edge, creating a thin stellar arc well distinct from the SF events that characterize the central disc. As soon as the satellite encounters ram-pressure values comparable to those experienced by the LMC at the perigalacticon (Time $\gtrsim$0.6 Gyr), some episodes of star formation occur even on the back side of the disc (last plot on the top right of Fig. 11), although they are not relevant in terms of the new stellar mass formed. Indeed, $M_\star$ shows a drastic drop at $\phi = 200°$.

Runs with inclination $i < 90°$ are characterized by significant star formation only for values of the external pressure larger than $10^{-13}\,\mathrm{dyn\,cm^{-2}}$. In the case of the nearly face-on run SF10, at $t >$ 0.7 Gyr star formation occurs in the entire external disc. Ram pressure affects the plane of the disc almost perpendicularly and stars form along the delocalized and filamentary high density structures visible in Fig. 9 (Mayer et al., in preparation). Contrary to what has been found by Kronberger et al. (2008) who focused on higher ram-pressure values ($n \sim 10^{-4}\,\mathrm{cm^{-3}}$ and $v = 1000\,\mathrm{km\,s^{-1}}$) typical of the outskirts of galaxy clusters, the newly formed stars are all located in the plane of the satellite's disc (with the exception of the high velocity face-on run SF10v400 where about 10 per cent of the stars forms behind the disc). The star formation events appear to be distributed nearly homogeneously along the azimuthal profile of the external disc, although a small peak in $M_\star$ is observable near $i = 90°$. In fact, the orientation of the disc with respect to its orbital motion is not exactly face-on. The case of the intermediate run SF45 is more complex. In a first phase, for low ram-pressure values, star formation is produced by compression at the leading edge and a thin star formation front – although not so well defined as in the case of a pure edge-on model – appears on the east side of the disc. As soon as the external pressure reaches a critical level, compression directed perpendicular to the disc becomes the dominant mechanism driving star formation.

Converting SFRs to Hα luminosities according to Kennicutt (1998):

$$L(\mathrm{H}\alpha) = \frac{\mathrm{SFR}(\mathrm{M_\odot\,yr^{-1}})}{1.26 \times 10^{41}}, \tag{8}$$

where SFR is the star formation rate averaged over the last 40 Myr (nearly two times the stellar age of 30 Doradus), we obtain the Hα maps illustrated in Fig. 12.

High emission regions are mainly concentrated on the external disc (with the exception of run SFld90 where the ram pressure exerted by the low density halo is not enough to induce star formation at the edge of the disc). The continuous stellar arc forming along the leading side of the disc in edge-on runs breaks up into several distinct and very luminous Hα regions that more closely resemble the star-forming complexes observed on the eastern border of the LMC. The inclusion of stellar and supernovae heating – which has been neglected in the present simulations – could prevent further star formation around highly emitting regions and consequently produce more compact and isolated star-forming complexes. Nevertheless, modelling single star-formation complexes – whose linear extension is smaller than our softening length – is beyond the scope of this paper.

The present inclination of the LMC's disc with respect to the orbital motion is about 60° (according to the convention adopted in this paper). Since the satellite is currently near a perigalactic passage, we expect the Hα map at the leading border of the disc to be something in between pure edge-on runs and the run with an inclination of 45°. On the other side, it is very likely that the disc inclination during the phase of approach to the pericentre was different. Indeed in Mastropietro (2008), we have simulated the LMC's orbit according to the new proper motion measurements of Kallivayalil et al. (2006). We found that in order to match the observed present-time inclination, the cloud has to enter the MW halo face-on. It moves almost face-on during most of the last 1 Gyr, turning nearly edge-on only at the perigalacticon, as a consequence of the orbital motion (the orbit is parabolic). This would have a remarkable effect on the star formation history of the external disc during the last 1 Gyr and some impact also on the Hα maps. Indeed, although the Hα emission would be mostly concentrated on the eastern side of the disc due to the very recent edge-on motion, we expect to see some luminous clumps forming a patchy distribution on the entire disc, due to gravitational instabilities and subsequent star formation induced by a nearly face-on compression of the gaseous disc before 30 Myr.

The high velocity edge-on run SF90v400 presents a more elongated and thinner stellar arc along the leading border, with a geometry similar to that obtained by increasing the SFR parameter to 0.05 (SF90c0.05). The Hα map of SF90v400 (third panel of the third row) shows two distinct luminosity peaks. One is located at the south-east region of the disc, roughly corresponding to the position of 30 Doradus and the two compact emission regions N159 and N160, respectively.

Fig. 13 illustrates how the SFR of the external disc changes with time in the different models. The three black curves refer to the standard star formation runs SF, characterized by low orbital velocities. The edge-on disc starts forming stars earlier, but for large

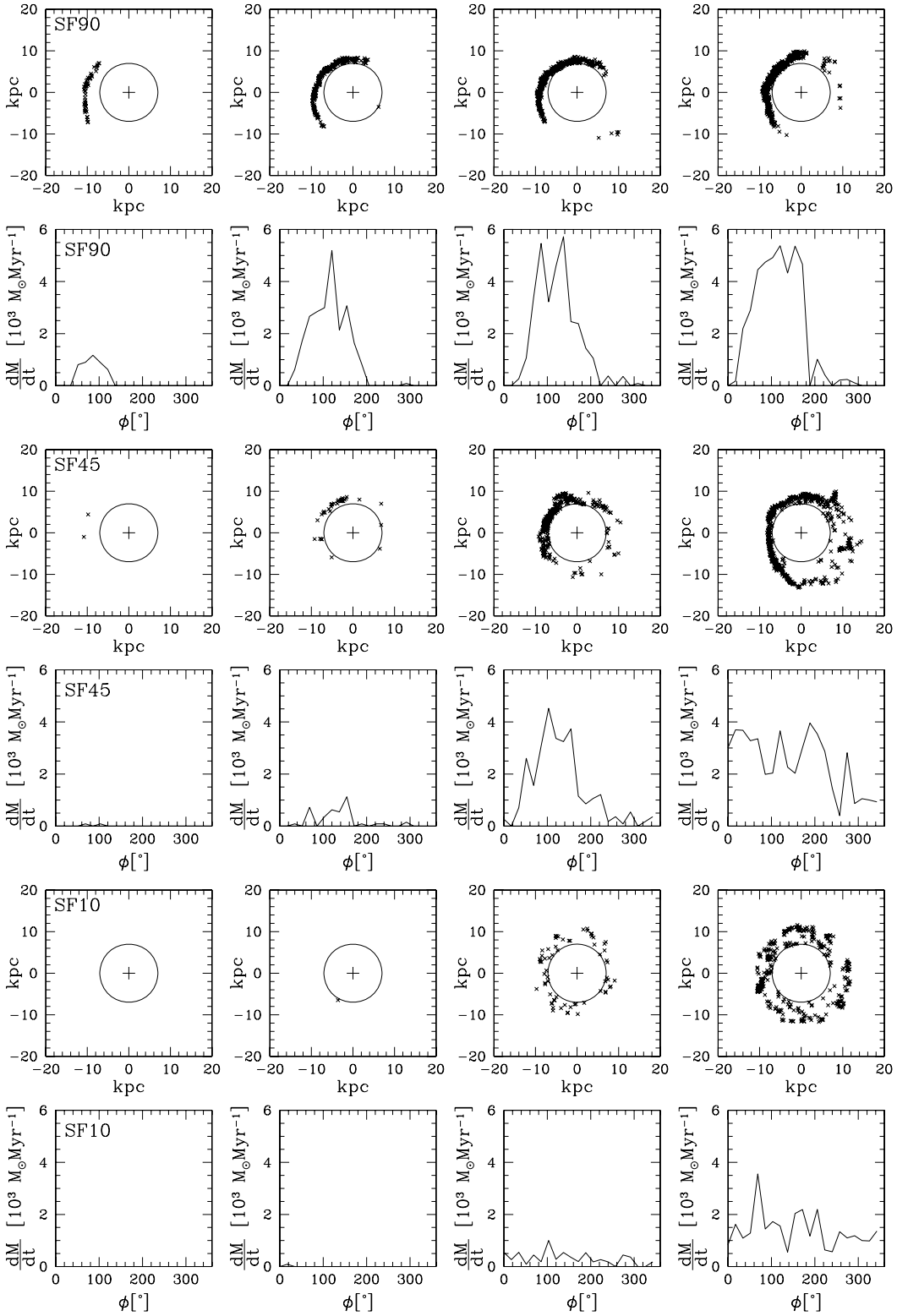

Figure 11. Location of the instantaneous SF events in the external disc. Each couple of rows corresponds to a different inclination angle of the disc. Time increases from the left to the right: Time = 0.4, 0.6, 0.8, 1 Gyr. The first row of the couple represents the disc face-on projection and the second one the SFR versus the azimuthal angle ϕ.

ram-pressure values the SFR of SF10 and SF45 grows faster. At the perigalacticon passage, SF45 has indeed a higher SFR than SF90. In the case of an isolated LMC model, star formation is almost absent for $r > 7$ kpc. The remaining curves in Fig. 13 refer to different SF recipes (rows 4–9 of Table 2). The location of the SF events in the external regions of the disc does not change significantly by choosing different parameters in the SF algorithm. The SFR parameter $c_\star$ determines the number of new stars forming but affects

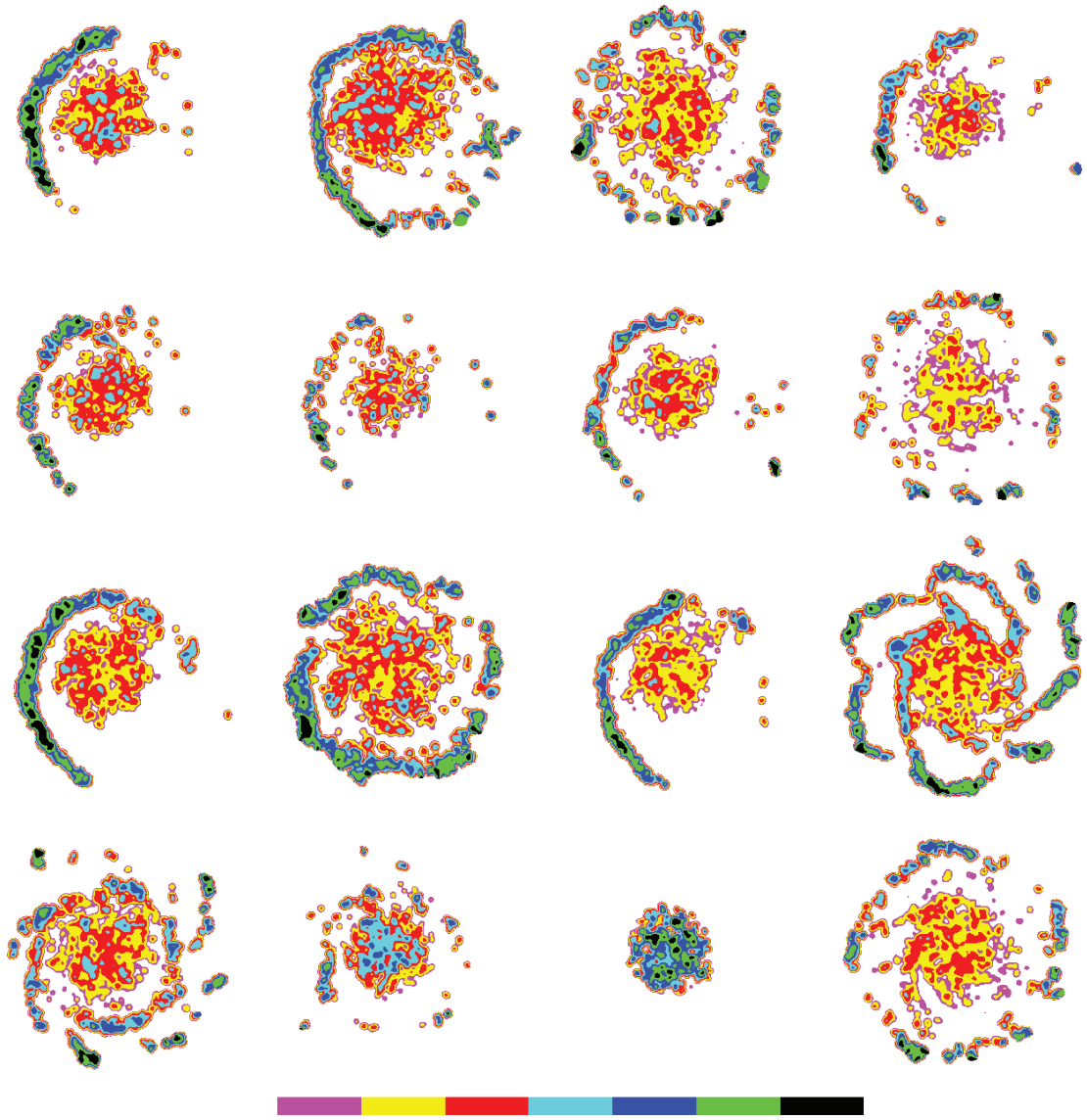

Figure 12. Hα maps of the LMC's disc. The different panels represent (from top to bottom and from left to right) runs listed in Table 2: SF90, SF45, SF10, SFconv, SFϵ1, SFconvϵ1, SF90c0.01, SF10c0.01, SF90c0.05, SF10c0.05, SF90v400, SF10v400, SF10v400t12000, SF10v400t15000, SFld90, SFld10. The colour scale is logarithmic with limits 10^{31} and 10^{34} erg s^{-1} kpc^{-2}.

neither the minimum threshold in ram pressure nor the evolution of the SFR. In particular, in the case of edge-on runs after an initial steep increment the curve seems to converge to a constant value for increasing external pressures. The consequences of an increased SF efficiency (ϵ1) are almost negligible (but not in Hα maps where only the very recent SFR is taken into account: compare the first panels of the first and second rows) while including the convergency requirement (SFconv) has nearly the same effect as reducing the SFR parameter by a factor of 2.

For convenience, the SFR of the last six runs of Table 2 is plotted separately (Fig. 14). The high velocity edge-on model SF90v400 is characterized by a steeper increment in SF at earlier times but later on the curve flattens and the SFR at the perigalacticon is similar to that of the low velocity case SF90. Differences in Hα maps are produced by a difference of $\sim 5 \times 10^3$ M$_\odot$ Myr^{-1} about Time = 1 Gyr. On the contrary, the SF generated by compression perpendicular to the disc increases with increasing ram-pressure values (it shows a decrement only towards the end of the simulation) and in the case of the high velocity run SF10v400 it reaches a peak $\sim$1.5 times higher than in SF10. The SFR of SF10v400 is strongly affected by the introduction of an artificial temperature threshold. With a temperature floor of 15 000 K, we nearly suppress SF in the external disc. However, a threshold of 12 000 K is already very high for an LMC model and more typical of luminous disc galaxies such as the MW. A temperature floor lower than 10 000 K would not make sense since below this temperature, the cooling function adopted in this paper drops rapidly to zero. If, as pointed out by Mastropietro (2008), the satellite is moving almost face-on until it gets very close to the perigalacticon, we would not expect to see SF before 0.6 Gyr independently of the orbital velocity. Differences between high and low velocity runs should be marginal also near the pericentre since SF in edge-on runs – assuming our standard prescriptions for SF – seems to saturate around $\sim 4 \times 10^4$ M$_\odot$ Myr^{-1}. Finally, a hot halo 10 times less dense than the one assumed in our favourite model would drastically reduce the SF in a face-on LMC and completely suppress the SF on the leading edge of the disc.

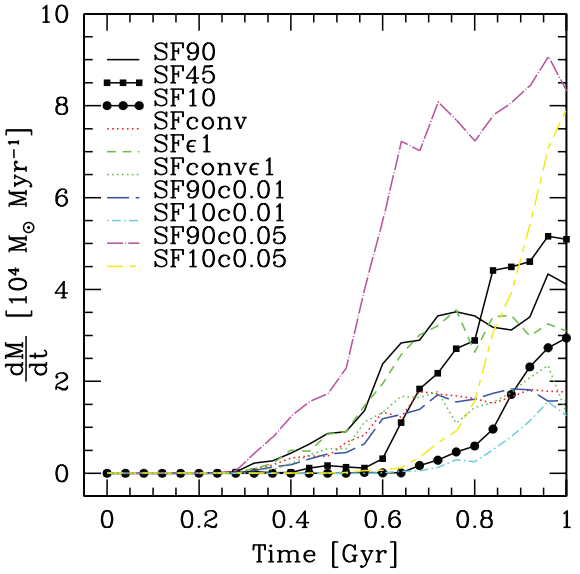

Figure 13. SFR of the external disc ϕ for the first 10 runs listed in Table 2. Time increases approaching the present position.

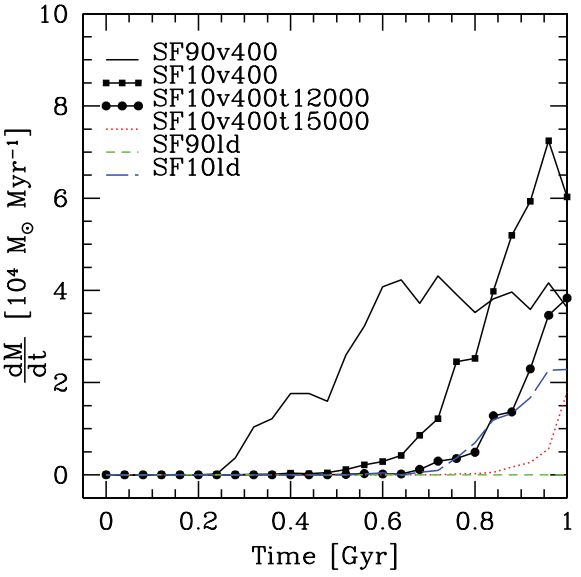

Figure 14. Same as in Fig. 13 for the last six runs listed in Table 2.

The SFR of the entire disc is illustrated in Fig. 15. This plot is only indicative since we neglect the presence of the bar and its influence on the SF history of the satellite. The SFR of an LMC model evolved in isolation is plotted for comparison. The largest contribution to the SFR is given by SF events in the central region of the disc. Curves peak between 15 and 35 $M_\odot$ Myr^{-1}, comparable with observations of the Magellanic Clouds Photometric Survey (Harris & Zaritsky 2009). The total SFR is clearly not affected by ram pressure before 0.4 Gyr. Indeed, after an initial sharp increment, curves are rather flat despite orientation and intensity of the external pressure. An initial burst in SF is obtained only by increasing the SF efficiency parameter to 0.05. For Time $>$ 0.5 Gyr the largest deviations from an average SFR of $\sim$15 $M_\odot$ Myr^{-1} are produced in the edge-on low density run SF90ld, where dM/dt drops to 10 $M_\odot$ Myr^{-1} at Time $=$ 1 Gyr, and in the high velocity face-on model SF10v400 whose SFR increases up to $\sim$24 $M_\odot$ Myr^{-1} towards the end of the

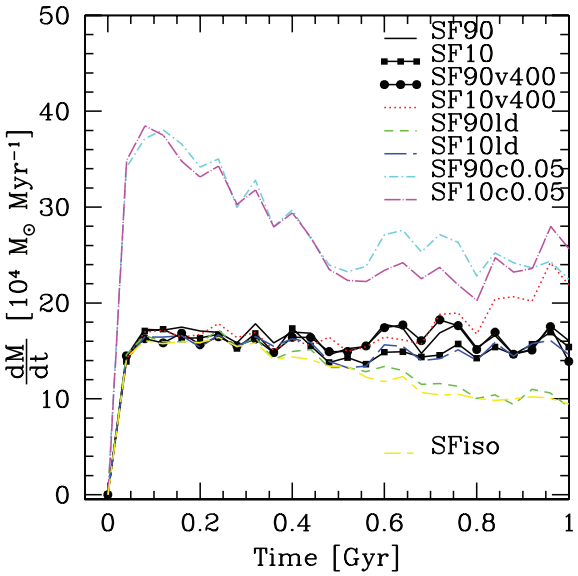

Figure 15. The SFR of the entire disc for selected runs in Table 2. SFiso refers to the LMC model run in isolation.

simulation. Differences among the other models are of the order of few $M_\odot$ Myr^{-1} and vary with time so that it would be quite difficult to use the SF history of the entire disc to test the Cloud's orbital parameters and the hot halo density.

Maps in Fig. 16 show the age distribution of newly forming stars in the disc, while Fig. 17 represents the mean stellar age of the external disc versus the azimuthal angle ϕ for the same selected runs of Fig. 15. The maximum increment in age in a clockwise direction is associated with edge-on runs, where stars forming at the leading edge move, in time, away to the side, due to the clockwise rotation of the disc. The youngest stars are located at $30^\circ < \phi < 100^\circ$. Clearly, the gradient in age is much weaker in models with $i < 90^\circ$. SF10v400 – with a mean stellar age of $\sim$250 Myr – forms stars earlier with respect to the other nearly face-on runs, while the difference between SF90v400 and the corresponding low velocity run SF90 is about 5 Myr at the leading edge and not significant in the rest of the external disc.

For the same runs, we also plotted the final radial gas density profile (Fig. 18). In most of the cases, a secondary peak is still present.

5 CONCLUSIONS

We have performed high-resolution 'wind tunnel' simulations to study the effects of ram pressure by a tenuous Galactic hot halo on the H I morphology of the LMC's disc, its recent SF history and location of the youngest star-forming regions. We did not focus on the mass loss produced by ram-pressure stripping since this would also be affected by tidal interactions. For the same reason, our galaxies do not form any bar and we actually start with a galaxy model very stable against bar formation so that the pure effects of external pressure are more clearly visible. On the other side we expect tidal forces to be symmetrical and affect the back side of the disc as much as the front, while observations indicate that the recent SF activity is mostly concentrated on the leading edge. Our LMC is a multicomponent system with a spherical NFW halo, an exponential stellar disc and a gaseous disc that extends up to eight times the stellar disc scalelength. In each simulation, the external flux of hot particles increases with time as the satellite approaches

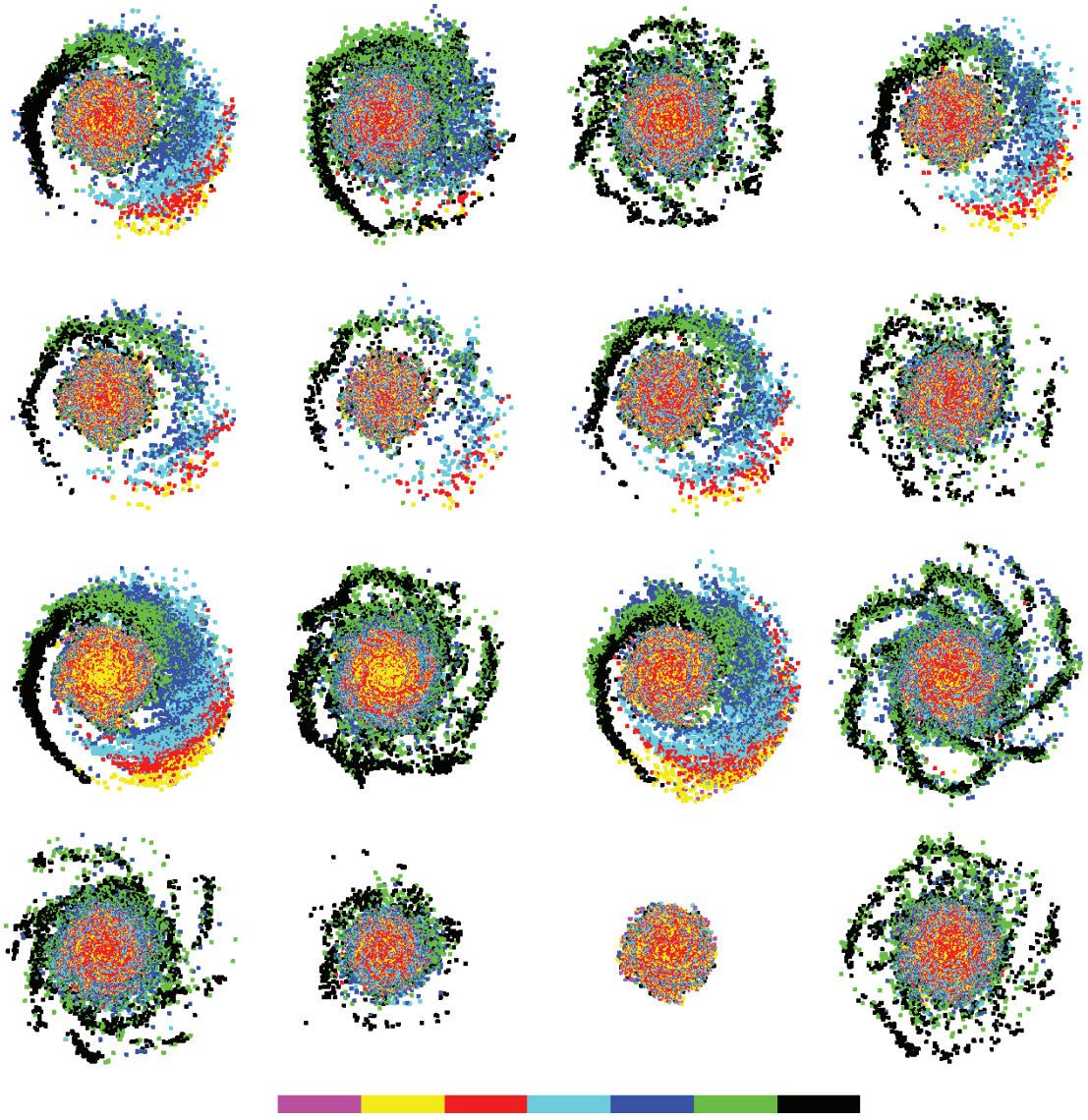

Figure 16. Age distribution of the newly forming stars in the LMC's disc. The different panels represent (from top to bottom and from left to right) runs listed in Table 2: SF90, SF45, SF10, SFconv, SFϵ1, SFconvϵ1, SF90c0.01, SF10c0.01, SF90c0.05, SF10c0.05, SF90v400, SF10v400, SF10v400t12000, SF10v400t15000, SFld90, SFld10. Magenta indicates stars older than 725 Myr.

the perigalacticon in such a way that the pressure experienced by the disc is consistent with the LMC's orbital velocity and an average hot halo density of $2 \times 10^{-5}\,\mathrm{cm}^{-3}$ within 150 kpc from the Galactic Centre. Low velocity runs are characterized by a 'classic' pericentric velocity of $300\,\mathrm{km\,s}^{-1}$ (M05) while high velocity runs have velocities compatible with the new proper motion measurements of Kallivayalil et al. (2006). We expect the angle between the LMC's disc and its proper motion to vary significantly during the last billion years of orbital interaction. We have defined the inclination angle i as the angle between the angular momentum vector of the disc and the flux of hot particles in the wind tube, so that the observed LMC's disc would have $i \sim 60^{\circ}$. Mastropietro (2008) performed self-consistent N-body/SPH simulations of the interacting system MW/LMC adopting orbital constraints from the last LMC's proper motion measurements and found that the Cloud enters the MW halo face-on ($i \sim 0^{\circ}$), moving nearly face-on for most of the last billion years. It turned edge-on only about 30 Myr ago. This means that the LMC is moving nearly edge-on close to the perigalactic passage, corresponding to the maximum ram-pressure values, consistently with the actual disc inclination measured by Kallivayalil et al. (2006).

We have performed several simulations varying the inclination angle of the disc, the SF recipe and the intensity of the external pressure. We have shown the following.

(i) The compression of the leading border of an edge-on LMC disc can account for the high density H I region observed at the south-east. In our simulations, this high density feature is well defined (with a mean density one order of magnitude higher than the surrounding gas) and localized within 1.5 kpc from the border of the disc. Its average thickness and velocity dispersion along the line of sight are larger than the average values in the rest of the disc. In cool90, it extends for almost 160° and could also explain the origin of the spiral arm E described by Staveley-Smith et al. (2003), which does not have an equivalent in the stellar disc.

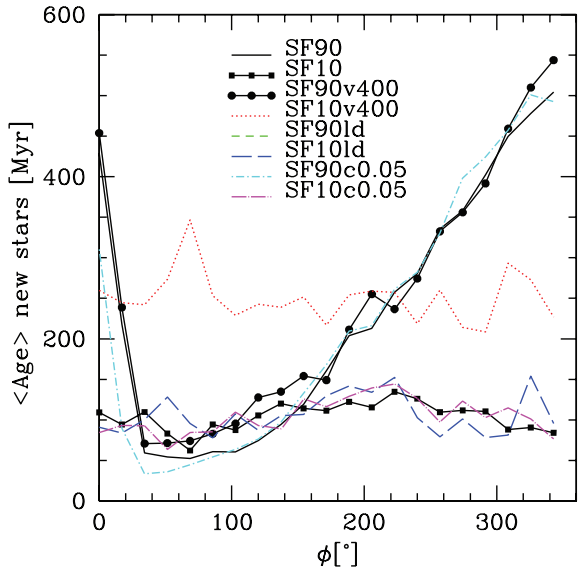

Figure 17. External disc mean stellar age as a function of the azimuthal angle ϕ for selected runs in Table 2.

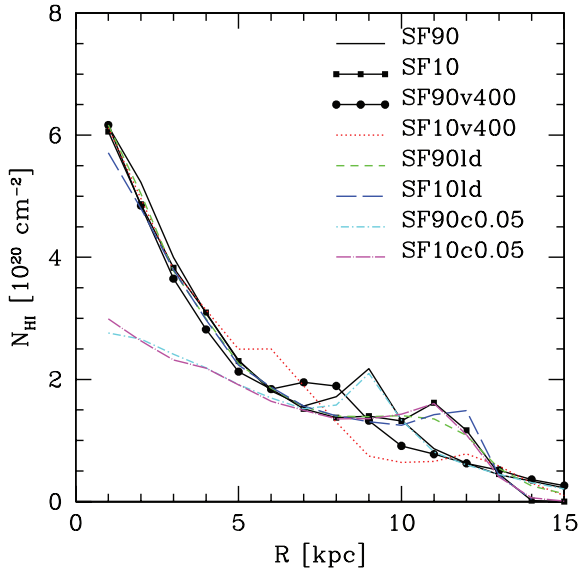

Figure 18. Azimuthally averaged H I column density profile of the final LMC disc for a selection of the runs listed in Table 2.

(ii) Compression directed perpendicular to the disc (in runs with $i < 90°$) produces local instabilities in the gas distribution and a clumpy structure characterized by voids and high density filaments similar to those observed by the Parkes multibeam H I survey (see fig. 3 of Staveley-Smith et al. 2003). If the satellite was moving nearly face-on in the past – and according to Mastropietro (2008) this is likely to happen during most of the LMC/MW orbital history – then ram pressure could be responsible for the general mottled appearance of the H I disc.

(iii) As a result of the increase in density along the edge of the disc, the mean H I column density shows a secondary peak at large radius, in agreement with observations.

(iv) The compression of the satellite's IGM is naturally associated with induced SF activity. We focused on the external regions of the disc since the central parts of the real LMC would be dominated by the bar. Edge-on discs start forming stars earlier, but for large ram-pressure values the SFR of runs with $i < 90°$ grows much faster. The high velocity edge-on model SF90v400 is characterized by a steeper increment in SF at earlier times but later on the curve flattens and the SFR at the perigalacticon is similar to that of the low velocity case SF90. On the other hand, the SF generated by a compression perpendicular to the LMC's disc increases with increasing ram-pressure values and in the case of the high velocity run SF10v400 it reaches a peak ∼1.5 times higher than in SF10. If the satellite is moving almost face-on until it gets very close to the perigalacticon, we would expect not to see SF before 0.6 Gyr independently of the orbital velocity. Differences between high and low velocity runs should be marginal also near the pericentre since SF in edge-on runs – assuming our standard prescriptions – seems to saturate around $\sim 4 \times 10^4\,\mathrm{M}_\odot\,\mathrm{Myr}^{-1}$.

(v) In edge-on models the SF of the external disc is characterized by a thin stellar arc along the leading border, well distinct from the SF events in the central disc. If the SFR is converted in Hα luminosities, this arc breaks in several distinct and very luminous Hα regions that more closely resemble the star-forming complexes observed on the eastern border of the disc. Although the Hα emission is mostly concentrated on the eastern side as a consequence of the very recent edge-on motion, we expect to see some luminous clumps forming a patchy distribution on the entire disc, due to gravitational instabilities and subsequent SF induced by a nearly face-on compression of the disc before 30 Myr. As observed by de Boer et al. (1998) stellar complexes on the leading edge show a progression in age in the clockwise direction, but a face-on compression in the recent past of the LMC would circumscribe this trend to the youngest stellar regions, with age < 30–40 Myr.

ACKNOWLEDGMENTS

We would like to thank M.-R. Cioni, T. Naab, T. Kaufmann and N. Kallivayalil for useful discussions. The numerical simulations were performed on the zBox1 supercomputer at the University of Zurich and on the local SGI-Altix 3700 Bx2 (partly funded by the cluster of excellence 'Origin and Structure of the Universe'). This work was partly supported by the DFG Sonderforschungsbereich 375 'Astro-Teilchenphysik'.

REFERENCES

Balsara D. S., 1995, J. Comput. Phys., 121, 357
Barnes J. E., 2002, MNRAS, 333, 481
Bekki K., Chiba M., 2005, MNRAS, 356, 680
Besla G., Kallivayalil N., Hernquist L., Robertson B., Cox T. J., van der Marel R. P., Alcock C., 2007, ApJ, 668, 949
Blondiau M. J., Kerp J., Mebold U., Klein U., 1997, A&A, 323, 585
Blumenthal G. R., Faber S. M., Flores R., Primack J. R., 1986, ApJ, 301, 27
Braun J. M., Bomans D. J., Will J.-M., de Boer K. S., 1997, A&A, 328, 167
Broeils A. H., van Woerden H., 1994, A&AS, 107, 129
Cioni M.-R. L., Girardi L., Marigo P., Habing H. J., 2006, A&A, 448, 77
Courteau S., 1997, AJ, 114, 2402
de Boer K. S., Braun J. M., Vallenari A., Mebold U., 1998, A&A, 329, L49
Evrard A. E., 1988, MNRAS, 235, 911
Fang T., Mckee C. F., Canizares C. R., Wolfire M., 2006, ApJ, 644, 174
Gerola H., Seiden P. E., 1978, ApJ, 223, 129
Grebel E. K., Brandner W., 1998, in Richtler T., Braun J. M., eds, The Magellanic Clouds and Other Dwarf Galaxies, Proc. Bonn/Bochum-Graduiertenkolleg Workshop. Shaker Verlag, Aachen, p. 151
Harris J., Zaritsky D., 2009, AJ, in press (arXiv:0908.1422)
Hernquist L., 1993, ApJ, 86, 389
Hunter D. A., Gallagher J. S. III, 1985, AJ, 90, 1789

Jog C. J., Solomon P. M., 1984, ApJ, 276, 114
Kallivayalil N., van der Marel R. P., Alcock C., Axelrod T., Cook K. H., Drake A. J., Geha M., 2006, ApJ, 638, 772
Katz N., 1992, ApJ, 391, 502
Katz N., Weinberg D. H., Hernquist L., 1996, ApJS, 105, 19
Kaufmann T., Mayer L., Wadsley J., Stadel J., Moore B., 2007, MNRAS, 375, 53
Kaufmann T., Bullock J. S., Maller A. H., Fang T., Wadsley J., 2009, MNRAS, 396, 191
Kennicutt R. C. Jr., 1989, ApJ, 344, 685
Kennicutt R. C. Jr., 1998, ApJ, 498, 541
Kronberger T., Kapferer W., Ferrari C., Unterguggenberger S., Schindler S., 2008, A&A, 481, 337
Maller A. H., Bullock J. S., 2004, MNRAS, 355, 694
Mastropietro C., 2009, in van Loon J. T., Oliveira J. M., eds, Proc. IAU Symp. 256, The Magellanic System: Stars, Gas, and Galaxies. Cambridge Univ. Press, Cambridge, p. 117
Mastropietro C., Moore B., Mayer L., Wadsley J., Stadel J., 2005, MNRAS, 363, 509 (M05)
Monaghan J. J., 1992, ARA&A, 30, 543
Monaghan J. J., Lattanzio J. C., 1985, A&A, 149, 135
Navarro J. F., Frenk C. S., White S. D. M., 1997, ApJ, 490, 493
Persic M., Salucci P., 1997, in Persic M., Salucci P., eds, ASP Conf. Ser. Vol. 117, Dark and Visible Matter in Galaxies and Cosmological Implications. Astron. Soc. Pac., San Francisco, p. 1
Piatek S., Pryor C., Olszewski E. W., 2008, AJ, 135, 1024
Putman M. E., Staveley-Smith L., Freeman K. C., Gibson B. K., Barnes D. G., 2003, ApJ, 586, 170
Rafikov R. R., 2001, MNRAS, 323, 445
Rasmussen J., Ponman T. J., Mulchaey J. S., 2006, MNRAS, 370, 453
Roediger E., Brüggen M., 2006, MNRAS, 369, 567
Roediger E., Brüggen M., 2007, MNRAS, 380, 1399
Sandage A., 1986, A&A, 161, 89
Silk J., in Peimbert M., Jugaku J., eds, Proc. IAU Symp. 115, Star Forming Regions. Reidel, Dordrecht, p. 663
Stadel J., 2001, PhD thesis
Staveley-Smith L., Kim S., Calabretta M. R., Haynes R. F., Kesteven M. J., 2003, MNRAS, 339, 87
Summers F. J., 1993, PhD thesis
Toomre A., 1964, ApJ, 139, 1217
van der Marel R. P., 2001, AJ, 122, 1827
van der Marel R. P., Alves D. R., Hardy E., Suntzeff N. B., 2002, AJ, 124, 2639
Vollmer B., Braine J., Pappalardo C., Hily-Blant P., 2008, A&A, 491, 455
Wadsley J. W., Stadel J., Quinn T., 2004, New Astron., 9, 137
Williams R. J. et al., 2005, ApJ, 631, 856

This paper has been typeset from a TEX/LATEX file prepared by the author.